This article has been accepted for publication in a future issue of this journal, but has not been fully edited. Content may change prior to final publication. Citation information: DOI 10.1109/TIA.2017.2695442, IEEE Transactions on Industry Applications

A General Analytical Three-Phase Induction Machine Core Loss Model in the Arbitrary Reference Frame

Yiqi Liu
Student Member, IEEE
University of Connecticut
Storrs, CT 06269, USA
yiqi.liu@uconn.edu

Ali M. Bazzi
Member, IEEE
University of Connecticut
Storrs, CT 06269, USA
alibazzi@ieee.org

***Abstract* [1] —An analytical three-phase induction machine model is proposed, derived, and validated in this paper. This model is capable for arbitrary *qd0*-frame analysis and core loss estimation at both line-fed and inverter-fed situations. Detailed model-based machine copper and core loss estimations are presented. A simulation verification of the model consistency is given under a changing load profile in MATLAB/ Simulink™. Then the model is verified comprehensively using three induction machines (1.5HP, 3HP, 10HP), where the model is proved to be scalable and to provide excellent machine loss estimation in line-fed situation and inverter-fed situation with machine input line filters as well as in the flux-weakening region. Finally, a series of sensitivity tests of the model parameters are performed and the effects of the parameters on the machine losses are discussed. It is believed that the proposed model will be beneficial for various *qd0*-frame model-based researches of three-phase induction machines.**

***Index Terms*—analytical model, core loss, iron loss, efficiency estimation, induction machine, induction motor, modeling**

I. INTRODUCTION

Induction machine models are extensively used in many industrial and academic fields including machine characterization and model extraction [1, 2], control design [3], fault detection [4], power electronics design [5], [6], loss minimization [7], and many others. Generally, machines are designed for full-load conditions where the copper loss is dominant. Core loss gradually takes the dominance as the load decreases. Therefore, incorporating core loss is important in the modeling of machines that frequently operate at relatively low-load conditions. But even under high-load conditions, considering core loss can lead to better estimates of a machine's total loss and efficiency, and render more accurate model-based analysis and control design.

Various induction machine models have been proposed in the literature for different applications. Two main models that are commonly used in the literature are: 1) The per-phase equivalent circuit [8], and 2) The dynamic three-phase model [9]. The first model is simple, but it cannot work in dynamic conditions neither perform *qd0*-frame transform, which is the basis of many advanced vector control algorithms. The second model does not have the same two issues as the first one, but it cannot estimate core loss or iron loss. There are several other analytical induction machine models in the literature. In [10], an arbitrary *qd0*-frame model is proposed with the core loss being expressed directly as parallel resistors in magnetizing branches of *d-q* equivalent circuits. But the model is proposed for steady-state vector controller design and the model accuracy is not provided. In [11] and [12], simplified *d-q* axis equivalent circuits are proposed for induction machine loss minimization control, where core loss resistor is immediately after/before the *q*-axis stator resistor, respectively. These simplified equivalent circuits ignore stator leakage inductance and are only valid in the rotor reference frame. A modified version of this model is proposed in [13] which includes leakage inductances. But the model still only works for rotor reference frame, and the core loss resistance is assumed to be independent of frequency. Moreover, elaborated induction machine models that use winding functions are applied in [15] and [16]. But these models are generally too complicated for controller design. Empirical models are also proposed in the literature, such as the classical Steinmetz's equation and its modified versions for core loss estimation [17], [18]. Similarly, induction machine total loss is modelled as a complex polynomial function of slip in [19]. These "black box" models are lack of internal interpretation, and are heavily rely on the accuracy and completeness of training data. Finite element analysis (FEA) [20], [21] and artificial intelligence (AI) [22] are also used in the model-based induction machine analysis. Compared to other types of models, analytical models are the most suitable for design of flux observers and machine controllers. For example, in the loss-minimization control design, the optimal control variable can be solved analytically, numerically or iteratively based on the analytical relationship between the machine loss and the control variable(s) [23-25].

The proposed induction machine model is a dynamic three-phase model that can perform *qd0*-frame processing and core loss estimation at the same time. This is achieved by applying the virtual core-loss resistance concept in the conventional dynamic three-phase model. The benefits and advantages of the proposed model are below:

- It can provide accurate core loss estimation in steady-state and dynamic conditions;
- It is capable for reference frame transformation which enables advanced *qd0*-frame analyses and designs;

[1] The work reported in this paper is partially supported by United Technologies Corporation (UTC) project number IASE-1311107, and a fellowship from the UTC Institute for Advanced Systems Engineering (UTC-IASE). Any opinions expressed in this paper are those of the authors and do not represent the sponsor. The authors acknowledge the support of Mr. Timothy Remmers from UTC.

This article has been accepted for publication in a future issue of this journal, but has not been fully edited. Content may change prior to final publication. Citation information: DOI 10.1109/TIA.2017.2695442, IEEE Transactions on Industry Applications

- It is a general model starting from *abc*-frame, and it can be transformed to an arbitrary *qd0*-frame as needed;
- It is a dynamic and analytical model; thus it is excellent for the design of flux observers and vector controllers;
- The parameters of the proposed model can be obtained conveniently from machine characterization tests based on the IEEE Standard 112-2004 [26].

Note that even though the proposed model uses parameters extracted from the steady-state characterization tests, the model itself is dynamic, which can deal with changing load conditions, as will be shown in Section III. Moreover, the focus of this paper is on introducing and validating the proposed model along with checking the model's parameter sensitivity. Implementing the proposed model in any specific applications, which may involve parameter adaptation of the model, is beyond the scope of this paper and is expected to be the future work. The detailed derivation of the proposed model is provided in Section II and the simulation verification is provided in Section III. The experimental validation and sensitivity tests are given in Sections IV and V, and Section VI concludes this paper.

II. Proposed Induction Machine Model

The proposed model is inspired by the conventional dynamic three-phase induction machine model and the per-phase equivalent circuit shown in Fig. 1 and Fig. 2, respectively. The proposed model is shown in Fig. 3. In Fig. 1, each phase branch consists of a resistance (R_s/R_r'), a self-inductance (L_{ls}/L_{lr}') and a magnetizing inductance (L_{ms}/L_{mr}'). Flux on each stator or rotor circuit is split into leakage and magnetizing parts, and only the latter part enters the magnetic coupling field. On the other hand, the per-phase equivalent circuit is much simpler. L_m is the mutual inductance which is equal to $1.5L_{ms}$. r_{c_ph} is the per-phase equivalent core-loss resistance. The proposed model in Fig. 3 has a similar structure as Fig. 1, which is also a dynamic three-phase model with resistance, self-inductance and magnetizing inductance in each phase branch. However, the stator magnetizing branches are modified by three virtual resistors, R_c, which are highlighted in red in Fig. 3. R_c is in parallel with L_{ms} in a similar manner as in the per-phase equivalent circuit. However, the later derivation will show that R_c and r_{c_ph} are not the same. Due to the injection of R_c, the stator phase currents are split into two parts: one for flux linkage generation via L_{ms} and the other one for core loss dissipation via R_c. Note that the rest of the stator circuit and the entire rotor circuit in Fig. 3 are the same as Fig. 1, which makes the *qd0*-frame manipulation of the proposed model convenient by referring to the similar process as in the conventional dynamic three-phase model.

A. Derivation of the qd0-Frame Forms of the Proposed Model and Loss Expressions

Taking phase *a* as an example, the phase voltage (v_{as}), current (i_{as}) and flux (λ_{as}) can be calculated based on Fig. 3,

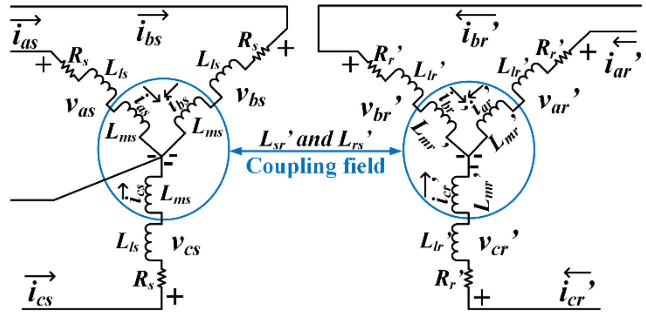

Fig. 1. The classical dynamic three-phase induction machine model ignoring core loss

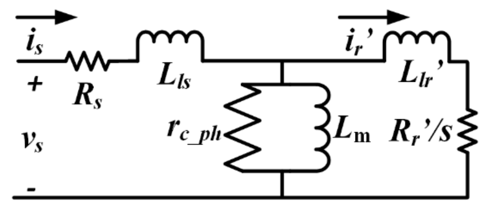

Fig. 2. The steady-state per-phase equivalent circuit of induction machines

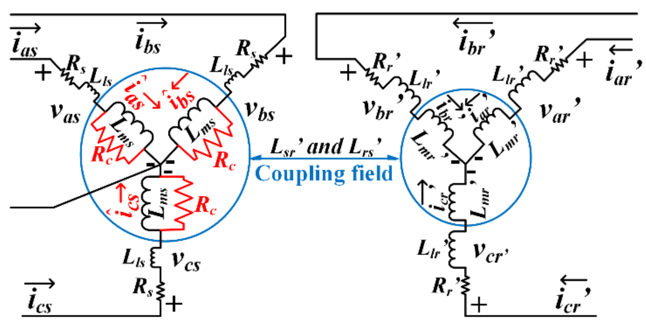

Fig. 3. The proposed induction machine model considering core loss

$$v_{as} = R_s i_{as} + p\lambda_{as} \ , \tag{1}$$

$$i_{as} = \hat{i}_{as} + \frac{L_{ms}}{R_c} p\hat{i}_{as} \ , \tag{2}$$

$$\begin{aligned}\lambda_{as} = &\left(L_{ls}i_{as} + L_{ms}\hat{i}_{as}\right) - 0.5L_{ms}\hat{i}_{bs} - 0.5L_{ms}\hat{i}_{cs} + L_{ms}\cos\theta_r i_{ar}' \\ &+ L_{ms}\cos\left(\theta_r + \frac{2\pi}{3}\right)i_{br}' + L_{ms}\cos\left(\theta_r - \frac{2\pi}{3}\right)i_{cr}'\end{aligned} \ , \tag{3}$$

where p is the derivative operator, θ_r is the rotor electrical angle. The other variables in (1) to (3) are illustrated in Fig. 3. Substituting i_{as} in (3) using (2) leads to a flux expression in terms of only magnetizing currents ($\hat{\boldsymbol{i}}_{abcs}$ and i_{abcr}'). Note that the stator magnetizing currents (the currents flowing through L_{ms}) are changed from $\boldsymbol{i}_{abcs}$ in Fig. 1 to $\hat{\boldsymbol{i}}_{abcs}$ in Fig. 3. Applying the same analysis to phase *b* and phase *c* as well as to phases on the rotor side, it leads to the voltage, current and flux relationships of the three-phase system in matrix forms,

$$\begin{pmatrix} \boldsymbol{v}_{abcs} \\ \boldsymbol{v}_{abcr}' \end{pmatrix} = \begin{pmatrix} \boldsymbol{R}_s & \boldsymbol{0} \\ \boldsymbol{0} & \boldsymbol{R}_r' \end{pmatrix} \begin{pmatrix} \boldsymbol{i}_{abcs} \\ \boldsymbol{i}_{abcr}' \end{pmatrix} + p \begin{pmatrix} \boldsymbol{\lambda}_{abcs} \\ \boldsymbol{\lambda}_{abcr}' \end{pmatrix}, \tag{4}$$

$$\begin{pmatrix} \boldsymbol{i}_{abcs} \\ \boldsymbol{i}_{abcr}' \end{pmatrix} = \begin{pmatrix} \hat{\boldsymbol{i}}_{abcs} \\ \boldsymbol{i}_{abcr}' \end{pmatrix} + \frac{L_{ms}}{R_c} \begin{pmatrix} p\hat{\boldsymbol{i}}_{abcs} \\ \boldsymbol{0} \end{pmatrix}, \tag{5}$$

This article has been accepted for publication in a future issue of this journal, but has not been fully edited. Content may change prior to final publication. Citation information: DOI 10.1109/TIA.2017.2695442, IEEE Transactions on Industry Applications

$$\begin{pmatrix}\boldsymbol{\lambda_{abcs}}\\ \boldsymbol{\lambda_{abcr}'}\end{pmatrix} = \begin{pmatrix}\boldsymbol{L_{ss}} & \boldsymbol{L_{sr}'}\\ \boldsymbol{L_{rs}'} & \boldsymbol{L_{rr}'}\end{pmatrix}\begin{pmatrix}\boldsymbol{\hat{i}_{abcs}}\\ \boldsymbol{i_{abcr}'}\end{pmatrix} + \frac{L_{ls}L_{ms}}{R_c}\begin{pmatrix}\boldsymbol{p\hat{i}_{abcs}}\\ \boldsymbol{0}\end{pmatrix}. \tag{6}$$

Here, bold font represents matrix variables. $\boldsymbol{F_{abcx}}=[F_{ax}\ F_{bx}\ F_{cx}]^T$, where F can represent voltage, current or flux while the subscript x can be s or r to represent stator or rotor components, respectively. The superscript T means transpose of a matrix. Detailed expressions of the matrixes $\boldsymbol{R_s}$, $\boldsymbol{R_r}'$, $\boldsymbol{L_{ss}}$, $\boldsymbol{L_{sr}}'$, $\boldsymbol{L_{rs}}'$ and $\boldsymbol{L_{rr}}'$ are referred to [8]. Transforming both sides of (4)-(6) into an arbitrary *qd0*-frame of frequency ω using the transformation matrix $\boldsymbol{K}$, where $\boldsymbol{F_{qd0x}}=\boldsymbol{K}\cdot\boldsymbol{F_{abcx}}$ and $\boldsymbol{\hat{i}_{qd0s}} = \boldsymbol{K}\cdot\boldsymbol{\hat{i}_{abcs}}$, $\boldsymbol{F_{qd0x}}=[F_{qx}\ F_{dx}\ F_{0x}]^T$, $\boldsymbol{\hat{i}_{qd0s}} =[\ \boldsymbol{\hat{i}_{qs}}\ \boldsymbol{\hat{i}_{ds}}\ \boldsymbol{\hat{i}_{0s}}\ ]^T$, $\boldsymbol{\hat{i}_{abcs}} =[\ \boldsymbol{\hat{i}_{as}}\ \boldsymbol{\hat{i}_{bs}}\ \boldsymbol{\hat{i}_{cs}}\ ]^T$, and

$$\boldsymbol{K} = \frac{2}{3}\begin{bmatrix} \cos\theta & \cos\left(\theta-\frac{2\pi}{3}\right) & \cos\left(\theta+\frac{2\pi}{3}\right)\\ \sin\theta & \sin\left(\theta-\frac{2\pi}{3}\right) & \sin\left(\theta+\frac{2\pi}{3}\right)\\ \frac{1}{2} & \frac{1}{2} & \frac{1}{2}\end{bmatrix},\quad \omega=\frac{d\theta}{dt}. \tag{7}$$

Then, the voltage, current and flux in the *qd0*-frame are obtained, which are shown in the Appendix A and referred as machine structural equations. These equations suggest the *qd0*-frame equivalent circuits as shown in Fig. 4. The impedances of Z_q and Z_d in Fig. 4 can be calculated by

$$Z_q = \frac{L_m p\left(\hat{i}_{qs}+i_{qr}'\right)}{i_{qs}-\hat{i}_{qs}}, \tag{8}$$

$$Z_d = \frac{L_m p\left(\hat{i}_{ds}+i_{dr}'\right)}{i_{ds}-\hat{i}_{ds}}. \tag{9}$$

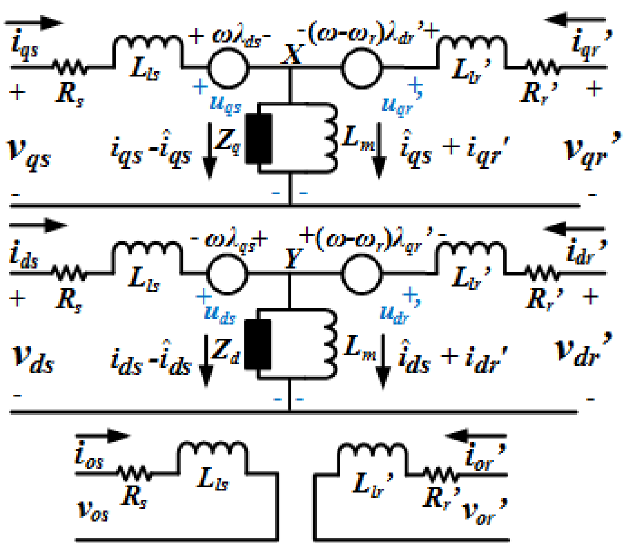

Fig. 4. The *qd0*-frame equivalent circuits of the proposed model

It is important to note that the *q*-axis and *d*-axis circuits in Fig. 4 are different from the per-phase equivalent circuit in Fig. 2. First, the impedance branches, Z_q and Z_d, are created only to satisfy the *KCL* law at nodes *X* and *Y*. They will contribute to the core loss, which is similar to r_{c_ph} in the per-phase equivalent model. However, they are not core loss resistances since the speed-voltage sources can also cause core loss in Fig, 4, as shown next. Second, there are extra speed-voltage sources in *q*-axis and *d*-axis circuits. Third, the rotor-side total resistance is no longer a function of *s*. The slip effect will be reflected in speed changing transients by

$$T_e - T_L = J\cdot p(\omega_{rm}), \tag{10}$$

where T_e and T_L are the induced electromagnetic torque and load torque, respectively. J is the machine inertia. T_e and T_L are equal at the steady state.

Assuming a balanced machine and thus ignoring the *0*-axis circuit in Fig. 4, copper loss can be calculated by the Joule losses on the stator and rotor resistors

$$P_{Cu} = \frac{3}{2}\left[R_s\left(i_{qs}{}^2+i_{ds}{}^2\right)+R_r'\left(i_{qr}'^2+i_{dr}'^2\right)\right], \tag{11}$$

where P_{Cu} is the copper power loss. The 3/2 coefficient is used to compensate the 2/3 factor in $\boldsymbol{K}$. By considering the energy flowing in the machine in instantaneous forms,

$$pW_e + pW_m = pW_{loss} + pW_{st}, \tag{12}$$

$$pW_{loss} = P_{Cu} + P_{core}, \tag{13}$$

$$pW_{st} = pW_{ss} + pW_{sm}, \tag{14}$$

where W_e, W_m, W_{loss}, W_{st} are the electrical input energy, mechanical input energy, dissipated or lost energy, and stored energy of the electro-mechanical field, respectively; W_{ss} and W_{sm} are the energy stored in the leakage flux and magnetizing flux, respectively. P_{core} is the core loss. p is again the derivative operator that converts energy to power. Based on (12)–(14) and Fig. 4,

$$\begin{aligned} P_{core} + pW_{sm} - pW_m &= pW_e - P_{cu} - pW_{ss}\\ &= \frac{3}{2}\left(u_{qs}i_{qs} + u_{qr}'i_{qr}' + u_{ds}i_{ds} + u_{dr}'i_{dr}'\right) \end{aligned}, \tag{16}$$

where, u_{qs}, u_{ds}, u_{qr}', u_{dr}' are shown in Fig. 4 (in blue). Expressing u_{qs}, u_{ds}, u_{qr}', u_{dr}' as functions of currents and fluxes, and then re-arranging the resultant terms,

$$\begin{aligned} &P_{core} + pW_{sm} - pW_m\\ &= \frac{3}{2}\begin{bmatrix} i_{qs}\cdot\omega\lambda_{ds} + i_{qr}'\omega\lambda_{dr}' + \left(i_{qs}-\hat{i}_{qs}\right)L_m\cdot p\left(\hat{i}_{qs}+i_{qr}'\right)\\ -i_{ds}\cdot\omega\lambda_{qs} - i_{dr}'\omega\lambda_{qr}' + \left(i_{ds}-\hat{i}_{ds}\right)L_m\cdot p\left(\hat{i}_{ds}+i_{dr}'\right)\end{bmatrix}\\ &+\frac{3}{2}\begin{bmatrix}\left(\hat{i}_{qs}+i_{qr}'\right)L_m\cdot p\left(\hat{i}_{qs}+i_{qr}'\right)\\ +\left(\hat{i}_{ds}+i_{dr}'\right)L_m\cdot p\left(\hat{i}_{ds}+i_{dr}'\right)\end{bmatrix} - \frac{3}{2}\omega_r\left(\lambda_{dr}'i_{qr}' - \lambda_{qr}'i_{dr}'\right) \end{aligned}. \tag{17}$$

Therefore, P_{core}, pW_{sm} and pW_m have the expressions as the three terms shown on the right side of (17) sequentially. Specifically, the expression of core loss is

This article has been accepted for publication in a future issue of this journal, but has not been fully edited. Content may change prior to final publication. Citation information: DOI 10.1109/TIA.2017.2695442, IEEE Transactions on Industry Applications

$$P_{core} = \frac{3}{2}\begin{bmatrix} i_{qs}\cdot\omega\lambda_{ds} + i_{qr}'\omega\lambda_{dr}' + \left(i_{qs} - \hat{i}_{qs}\right)L_m\cdot p\left(\hat{i}_{qs} + i_{qr}'\right) \\ -i_{ds}\cdot\omega\lambda_{qs} - i_{dr}'\omega\lambda_{qr}' + \left(i_{ds} - \hat{i}_{ds}\right)L_m\cdot p\left(\hat{i}_{ds} + i_{dr}'\right)\end{bmatrix}. \quad (18)$$

Equation (18) is the general expression of P_{core} that works for any arbitrary $qd0$-frame. In the synchronous $qd0$-frame where $\boldsymbol{i}_{qd0s}$, $\boldsymbol{i}_{qd0r}'$ and $\hat{\boldsymbol{i}}_{qd0s}$ are constant at steady state, the derivative terms in (18) are zero and P_{core} can be simplified to

$$\begin{aligned} P_{core\_syn} &= \frac{3}{2}\left(i_{qs}\cdot\omega_e\lambda_{ds} + i_{qr}'\omega_e\lambda_{dr}' - i_{ds}\cdot\omega_e\lambda_{qs} - i_{dr}'\omega_e\lambda_{qr}'\right) \\ &= \frac{3}{2}\frac{\omega_e^2 L_m L_{ms}}{R_c}\left(\hat{i}_{ds}^2 + \hat{i}_{ds}i_{dr}' + \hat{i}_{qs}^2 + \hat{i}_{qs}i_{qr}'\right) \end{aligned}, \quad (19)$$

where P_{core_syn} and ω_e are the synchronous $qd0$-frame core loss and synchronous frequency, respectively. Note that (19) is provided for the reader's convenience for line-fed core loss estimation in synchronous $qd0$ frame, it cannot be used in inverter-fed condition or line-fed but non-synchronous $qd0$ frame, whereas (18) can be used in all cases. On the other hand, T_e and ω_{rm} can be calculated by (20) and (10), respectively.

$$T_e = -\frac{pW_m}{\omega_{rm}} = \frac{3P}{4}\left(\lambda_{qr}'i_{dr}' - \lambda_{dr}'i_{qr}'\right). \quad (20)$$

B. Determination of the Proposed Model Parameters

As shown in Fig. 3, there are six independent parameters in the proposed model: R_s, L_{ls}, R_r', L_{lr}', R_c and L_{ms} ($L_{sr}'=L_{rs}'=L_m=1.5L_{ms}$). The determination of these parameters can follow the IEEE Standard [26]. Although the machine characterization tests, namely the DC test, locked-rotor test and no-load test, are designed to extract the parameters of the per-phase equivalent circuit model, the derivation next will show that the parameters in the proposed model are the same as the parameters in the per-phase equivalent circuit (that is why the same symbols are used in Fig. 2 and Fig. 3), except r_{c_ph} which is equal to 1.5 R_c instead of R_c.

Starting with the phasor forms of (A-1) and (A-3) by replacing p by $j(\omega_e$-$\omega)$, then using the $qd0$-frame phasor property $\tilde{F}_{dx} = j\tilde{F}_{qx}$, where the tilde sign means the quantity in phasor form. The phasor forms of (A-1) and (A-3) are,

$$\tilde{V}_{qs} = R_s\tilde{i}_{qs} + j\omega_e\tilde{\lambda}_{qs}, \quad (21)$$

$$\tilde{V}_{qr}' = R_r'\tilde{i}_{qr}' + j\left(\omega_e - \omega_r\right)\tilde{\lambda}_{qr}'. \quad (22)$$

Applying the phasor forms of (A-7) and (A-9) to (21) and (22), and using another phasor property, $\tilde{F}_{qx} = \tilde{F}_{ax}$, to current terms by selecting the initial phases of i_{as}, i_{ar}, $\hat{i}_{as}$ to be zero,

$$\tilde{V}_{as} = \left(R_s + j\omega_e L_{ls}\right)\tilde{i}_{as} + j\omega_e L_m\left(\tilde{\hat{i}}_{as} + \tilde{i}_{ar}'\right), \quad (23)$$

$$\frac{\tilde{V}_{ar}'}{s} = \left(\frac{R_r'}{s} + j\omega_e L_{lr}'\right)\tilde{i}_{ar}' + j\omega_e L_m\left(\tilde{\hat{i}}_{as} + \tilde{i}_{ar}'\right). \quad (24)$$

Equations (23) and (24) represent the steady-state per-phase version of the proposed model that is shown in Fig. 5. The resistance branch, r_{c_ph}, is created to satisfy the KCL law at node A. The same resistance symbol, r_{c_ph}, is used in Fig. 5 as in Fig. 2, since it is found that Fig. 5 and Fig. 2 are essentially the same considering $\tilde{V}_{ar}$ is zero in a squirrel-cage induction machine. Based on Fig. 5, r_{c_ph} can be calculated by

$$r_{c\_ph} = \frac{j\omega_e L_m\left(\tilde{\hat{i}}_{as} + \tilde{i}_{ar}'\right)}{\tilde{i}_{as} - \tilde{\hat{i}}_{as}}. \quad (25)$$

Using the phasor form of (A-5) and applying the previous phasor properties to change the q-axis and d-axis phasors to the a-axis, equation (25) is changed to

$$r_{c\_ph} = \frac{3}{2}R_c\frac{\tilde{\hat{i}}_{as} + \tilde{i}_{ar}'}{\tilde{\hat{i}}_{as}}. \quad (26)$$

In the no-load machine characterization test, the induced rotor current is negligible. Thus, (26) can be simplified to

$$R_c \cong \frac{2}{3}r_{c\_ph}\ \text{(no load)}. \quad (27)$$

Therefore, R_c of the proposed model can be obtained based on the $r_{c\text{-}ph}$ value from the no-load characterization test. Note that as r_{c_ph} changes with frequency and flux levels, the same to R_c. This point will be shown in Section IV.

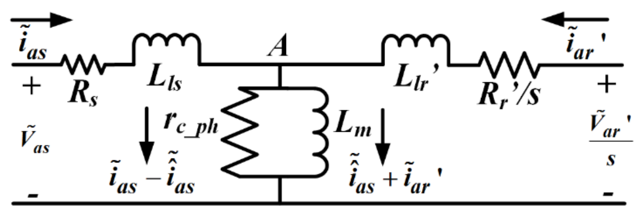

Fig. 5. The steady-state per-phase version of the proposed model

III. SIMULATION VERIFICATION

To verify the proposed, especially the analytical expression of P_{core}, a simulation is built in MATLAB/Simulink™, where the consistency of the model is checked based on

$$P_{in}\left(elec\right) - P_{out}\left(mech\right) = P_{Cu} + P_{core} + pW_{st} + P_{mech}. \quad (28)$$

P_{mech} is the mechanical loss, whose determination will be introduced in Section IV. The instantaneous stored energy can be averaged out if applying an average window longer than the fundamental period of the power source on both sides of (28) (pW_{st}=0).

A. Simulation Verification in Line-fed Situations

The high-level block diagram of the simulation verification in the line-fed situation is shown in Fig. 6. P_{in} and P_{out} are calculated by

This article has been accepted for publication in a future issue of this journal, but has not been fully edited. Content may change prior to final publication. Citation information: DOI 10.1109/TIA.2017.2695442, IEEE Transactions on Industry Applications

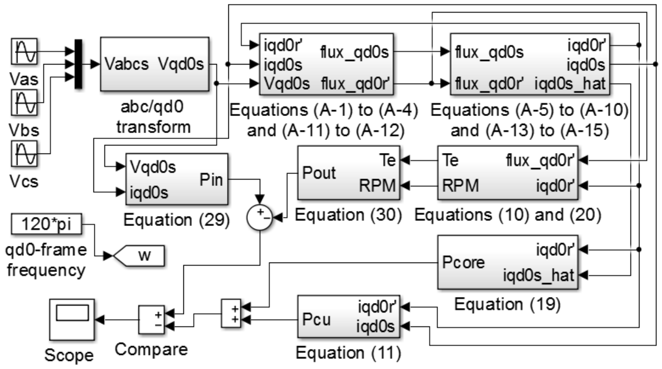

Fig. 6. Simulink simulation of the proposed model in line-fed situation

$$P_{in} = \frac{3}{2}\left(v_{qs}i_{qs} + v_{ds}i_{ds}\right), \tag{29}$$

$$P_{out} = T_e \omega_{rm} . \tag{30}$$

To check the validity of (28), a linearly increasing load torque followed by several step-down load torques is applied. The result is shown in Fig. 7(left). It is found that (P_{Cu}+P_{core}) is almost the same as (P_{in}–P_{out}) except at the load step-down instances. The zoomed-in figure of P_{in} and P_{out} at 9s is shown in Fig. 7(right) which explains the reason of the spikes: P_{out} is decreased instantaneously at 9s due to the change of the load torque command, whereas P_{in} has a responding transient due to machine inertia. The little delay of P_{in} leads to the spikes when calculating the difference between P_{in} and P_{out}. However, the loss estimation (P_{Cu}+P_{core}) of the proposed model does not have the issue. The individual copper and core losses are shown in Fig. 8. Both P_{core} and P_{Cu} follow the same changing trend as the load, but the changing degree of P_{core} is very small, since P_{core} is more a function of flux level. Moreover, P_{Cu} is the main component of the total power loss at high-load conditions, but P_{core} gradually dominates when the load decreases.

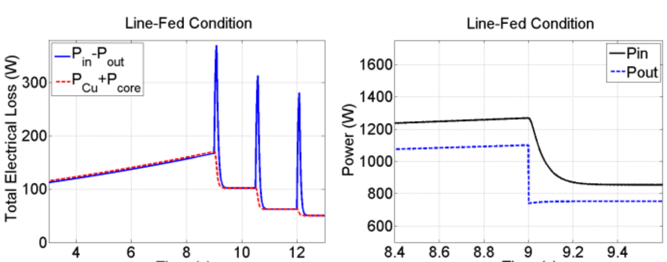

Fig. 7. Comparison of (P_{in}–P_{out}) and (P_{Cu}+P_{core}) in the line-fed situation (left); Zoomed-in version of P_{in} and P_{out} around 9s (right)

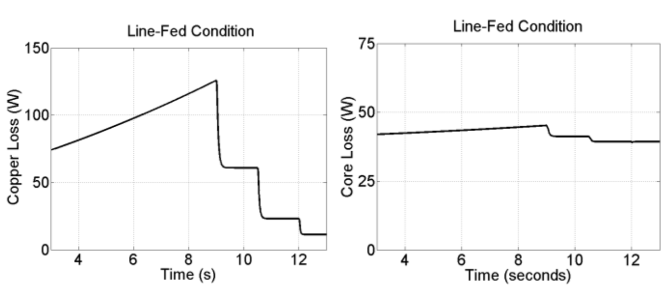

Fig. 8. The simulated machine copper loss (left) and core loss (right)

B. Simulation Verification in Inverter-fed Situations

Compared to the line-fed situation, there are two changes in the inverter-fed simulation. First, PWM voltage sources are used as the machine input. Second, the core loss is calculated using (18) instead of (19), where all the derivative terms are kept. A moving average window is applied to the power estimations in order to eliminate the large transients due to the derivative terms and the PWM voltages. In order to prove that the proposed model works for different *qd0*-frames at different speeds, the synchronous and stationary *qd0*-frames are each tested at three speeds (1735RPM, 1200RPM, 600RPM). The results are shown in Figs. 9-11. (P_{Cu}+P_{core}) is found to match (pW_e –pW_m) closely, except at the load step-down instances as in the line-fed situation. Since the same torque change will lead to larger power change in high-speed conditions, the spikes are larger for higher speeds in Figs. 9-11. It is also noted that the loss estimation in the synchronous and stationary *qd0*-frames are the same as expected.

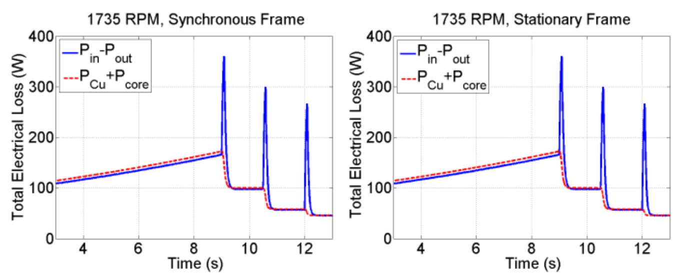

Fig. 9. Comparison of (P_{in}–P_{out}) and (P_{Cu}+P_{core}) in inverter-fed situation at 1735 RPM in synchronous *qd0* frame (left) and stationary *qd0* frame (right)

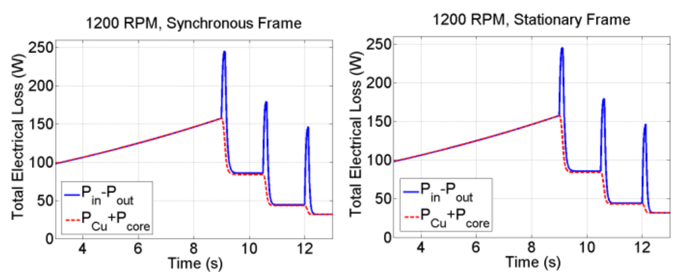

Fig. 10. Comparison of (P_{in}–P_{out}) and (P_{Cu}+P_{core}) in inverter-fed situation at 1200 RPM in synchronous *qd0* frame (left) and stationary *qd0* frame (right)

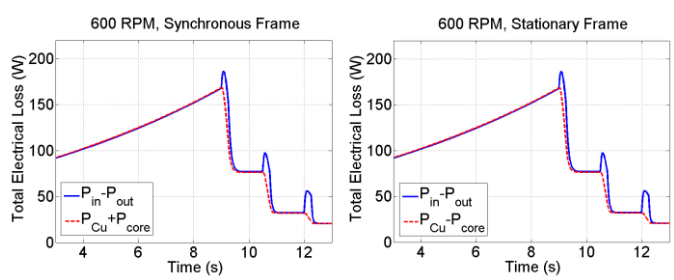

Fig. 11. Comparison of (P_{in}–P_{out}) and (P_{Cu}+P_{core}) in inverter-fed situation at 600 RPM in synchronous *qd0* frame (left) and stationary *qd0* frame (right)

IV. EXPERIMENTAL VALIDATION

In the experimental validation, the simulated and experimental machine losses are compared at no-load conditions. Three induction machines (1.5HP, 3HP and 10HP)

This article has been accepted for publication in a future issue of this journal, but has not been fully edited. Content may change prior to final publication. Citation information: DOI 10.1109/TIA.2017.2695442, IEEE Transactions on Industry Applications

are tested to show the scalability of the proposed model. The basic information of these machines is provided in Appendix B. The model validity under line-fed and inverter-fed situations as well as in the flux-weakening regions are studied. In the inverter-fed situation, each of the three induction machines are tested under seven different speeds while the V/f ratio is kept constant. As in many literatures which deal with core loss model verification, no-load condition is selected since the stray loss and rotor copper loss are small enough to be reasonably neglected [27-30]. On the other hand, the practically inevitable mechanical loss, P_{mech}, due to friction and windage needs to be considered to increase the model accuracy. P_{mech} can be determined experimentally following IEEE Standard 112-2004 [26]—Basically, several no-load tests are performed under a certain speed with different voltage excitations decreased from the rated voltage. Then, the power (P_{core}+P_{mech}) versus voltage excitation can be curve-fitted by a second-order polynomial equation. The extrapolation of the curve at *y*-axis gives P_{mech} for that speed. Examples of such curves for the 1.5HP machine under the seven different speeds are shown in Fig. 12, while P_{mech} of the tested machines at different speeds are shown in Fig. 13.

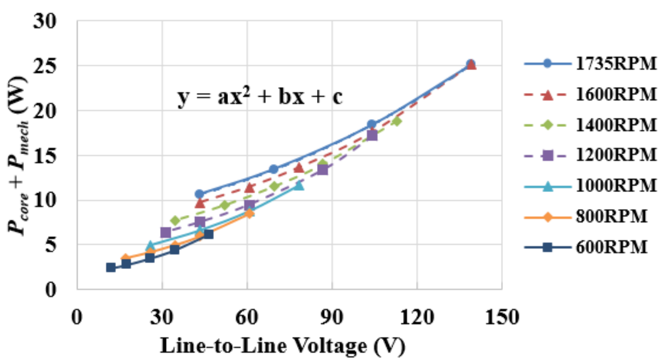

Fig. 12. Determination of P_{mech} for the 1.5HP induction machine

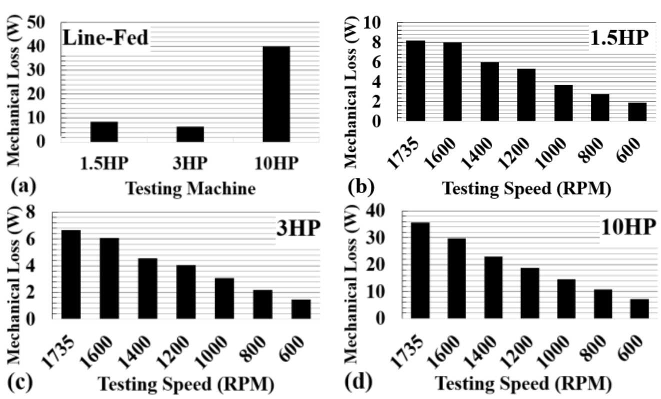

Fig. 13. Mechanical losses: (a) Line-fed situation (60Hz) for the three testing machines; (b) 1.5HP machine at seven speeds; (c) 3HP machine at seven speeds; (d) 10HP machine at seven speeds

A. Experimental Validation in Line-Fed Situation

The induction machine characterization tests are used to extract the proposed model parameters. The block diagram of the test rig for the line-fed situation is shown in Fig. 14. The induction machines are energized by grid via a variable AC source (VARIAC). A Kollmorgen AKM™ servomotor is used as a dynamometer which locks the machine rotor at the lock-rotor test and is decoupled from the induction machine at the no-load test to minimize mechanical losses. Yokogawa WT1800™ power analyzer is used to measure the machine input voltage, current and power. The experimental core loss is calculated by subtracting the stator copper loss and the pre-determined mechanical loss from the measured machine input power, since the rotor copper loss and stray loss are assumed to be zero in the no-load condition. The experimental and simulated machine losses are compared in Fig. 15. It is evident that the proposed model has excellent accuracy in loss estimation in the line-fed situation.

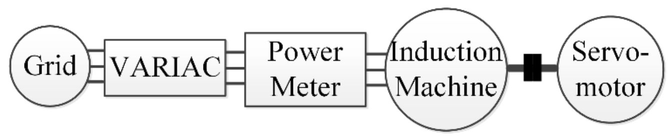

Fig. 14. Block diagram of the test rig for the machine characterization test and model validation in line-fed situation

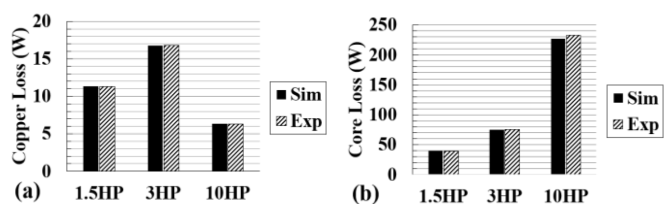

Fig. 15. The comparison of simulated and experimental machine losses in the line-fed situation: (a) Copper loss; (b) Core loss

B. Experimental Validation in Inverter-Fed Situation

The block diagram of the test rig for the inverter-fed situation is shown in Fig. 16 and the real experimental setup is shown in Fig. 17. dSPACE DS1104™ is used to provide real-time PWM switching signals from a V/f controller built in MATLAB/Simulink™. Each machine is tested under seven different speeds: 1735(for the 1.5HP and 3HP machines)/1755(for the 10HP machine), 1600, 1400, 1200, 1000, 800 and 600 RPM. Experimental machine losses are again calculated from the power analyzer's measurements: 1) Using current measurement and known stator resistance to calculate copper loss; 2) Subtracting the copper loss and the pre-determined mechanical loss from the input power to get the experimental core loss in no-load conditions.

Considering that some of the model parameters are functions of speed, machine characterization tests under different speeds are performed to extract the corresponding model parameters. This is accomplished by using a variable-frequency AC power supply (Pacific 320AMX™) which can output three-phase sinusoidal voltages with independent magnitude and frequency settings. It is found that the change of R_s, L_{ls}, L_{lr}' and L_m/L_{ms} with respect to the operating speed/frequency is negligible, while the operating speed mainly affects R_c, as shown in Fig. 18. Moreover, R_r' slightly increases with speed in Fig. 18 due to imperfect estimation of P_{mech} and inclusion of tiny excess losses in reality during the calculation of R_r'. On the other hand, higher-order harmonics in PWM excitation will also modify the model parameters

This article has been accepted for publication in a future issue of this journal, but has not been fully edited. Content may change prior to final publication. Citation information: DOI 10.1109/TIA.2017.2695442, IEEE Transactions on Industry Applications

beyond the values determined by the fundamental component. Therefore, the model parameters obtained from sinusoidal-fed characterization tests could be inaccurate for the corresponding inverter-fed conditions depending on the harmonics' levels. But note that this inaccuracy is induced by the parameters' values instead of the model itself. Better accuracy of loss estimation is expected with inverter-fed characterization tests. However, no standard is currently available to instruct such tests and we stick with the sinusoidal-fed tests to extract model parameters. To alleviate the impacts of the harmonics, low pass filters (LPFs) are used at the input of the machines. The simulated and experimental machine losses in the inverter-fed conditions are compared in Fig. 19, and the estimation error is shown in Fig. 20. Note that the results of the 3HP machine at 800 RPM and 600 RPM, and the 10HP machine at 600 RPM are not obtained experimentally due to the stall of machine. It is observed that the proposed model can estimate machine total loss with higher than 93% accuracy for all the tested conditions on the three machines, and the estimation errors for many conditions are less than 2%. Moreover, even without LPFs, the proposed model still can provide better than 80% estimation accuracy of machine losses under the present level of harmonics (1kHz PWM switching frequency).

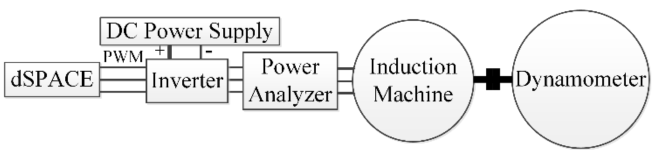

Fig. 16. Block diagram of the test rig for inverter-fed tests

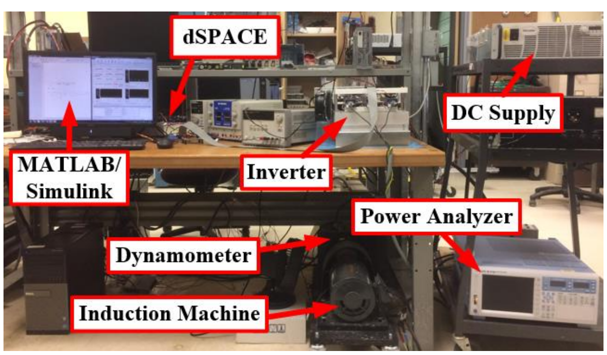

Fig. 17. The real experiment setup for inverter-fed tests

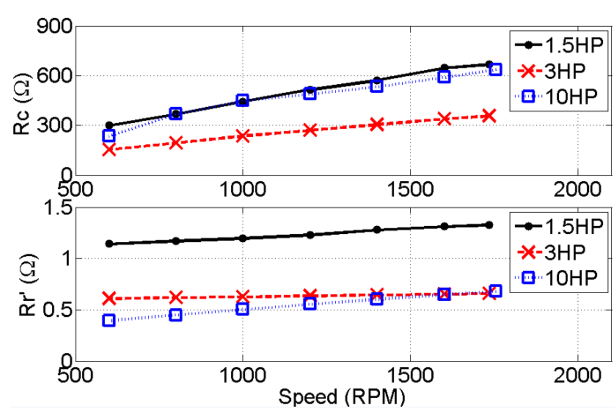

Fig. 18. Change of the model parameters at different speeds

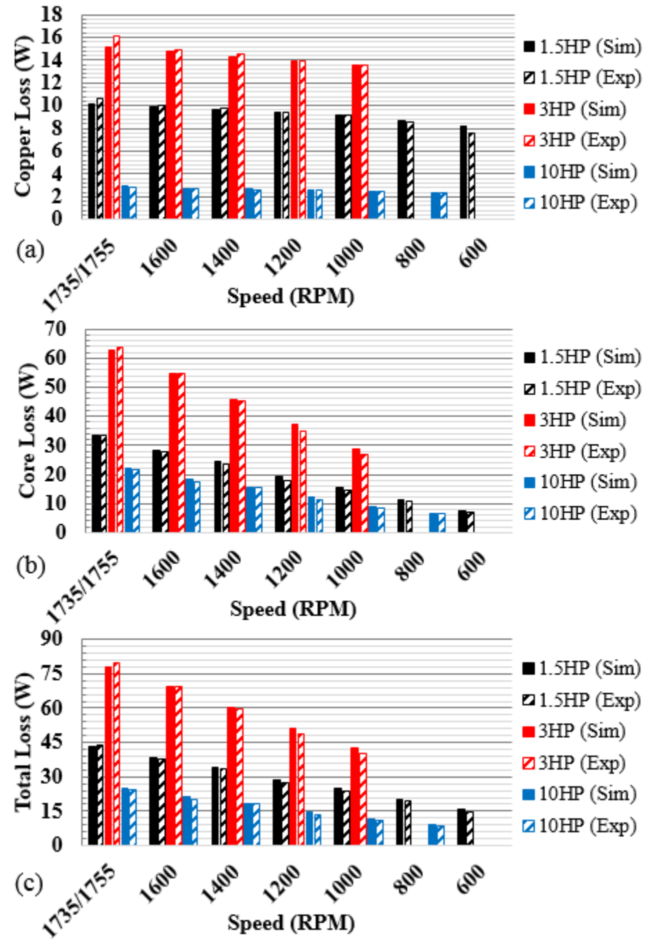

Fig. 19. Comparison of the simulated and experimental machine losses under inverter-fed conditions: (a) Copper loss; (b) Core loss; (c) Total loss

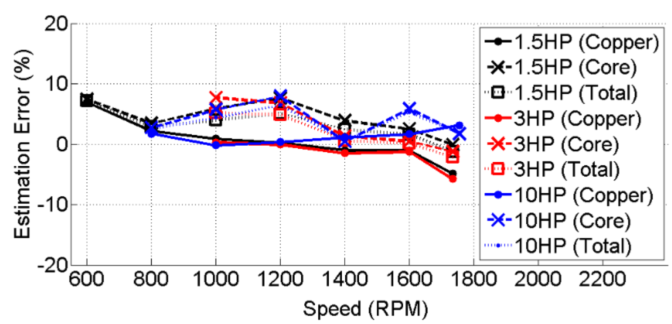

Fig. 20. The power loss estimation error of the proposed model at inverter-fed conditions

Compared to sinusoidal voltage source, PWM excitation induces additional machine copper and core losses, or PWM harmonic losses, due to the higher harmonics as well as possible negative thermal effects and change in the machine's operating point [31]. It is indicated in [28] that the PWM harmonic copper loss is typically larger than the PWM harmonic core loss at the low-frequency end of the harmonic spectrum, but it decreases fast and can be neglected at high harmonic frequencies. The hysteresis loss component of the PWM core loss is approximately inversely proportional to switching frequency [32]. If skin effect is considered, the

This article has been accepted for publication in a future issue of this journal, but has not been fully edited. Content may change prior to final publication. Citation information: DOI 10.1109/TIA.2017.2695442, IEEE Transactions on Industry Applications

PWM harmonic core loss will decrease slightly with harmonic frequency at high frequencies, and the decrease of the PWM harmonic copper loss with frequency will be significantly slower. Note that the PWM losses and skin effects are not treated explicitly in the proposed model, but their effects can be accommodated if the model parameters are extracted from corresponding characterization tests.

C. Experimental Validation under Flux Weakening

The proposed model is further verified under flux-weakening region using the Pacific 320AMX™ AC power supply and the 1.5HP motor. In this test, the speed of the machine is fixed at 1200 RPM and the V/f ratio is decreased from the rated value until the speed drops significantly. As some of the model parameters are functions of the flux level, the characterization tests are performed under the flux-weakening region to obtain more accurate model parameters. It is found that R_s, L_{ls}, R_r' and L_{lr}' are almost independent of the flux level. R_c increases slightly with the drop of the V/f ratio at first; it is then stabilized at the increased value for further decrease of the flux level. L_m increases for light flux weakening and then decreases for heavy flux weakening that forms a parabolic curve, as shown in Fig. 21. The comparison of simulated and experimental copper and core losses in the flux-weakening region are shown in Fig. 22, where the proposed model displays excellent loss estimation.

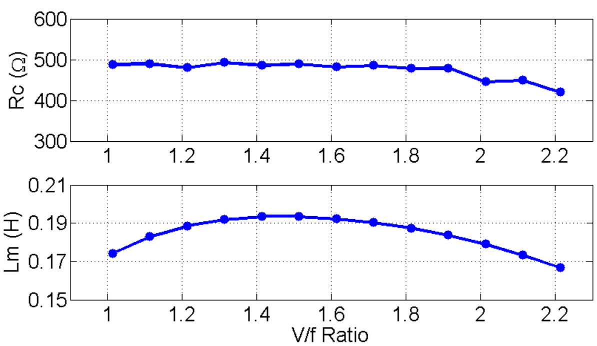

Fig. 21. Change of the model parameters at different flux levels

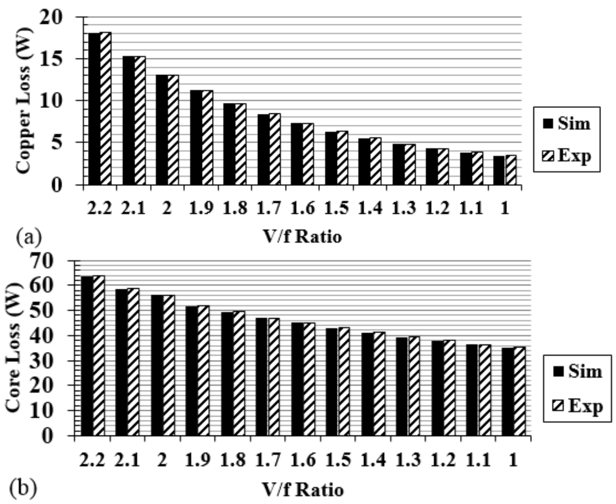

Fig. 22. Comparison of the simulated and experimental machine losses in the flux-weakening region: (a) Copper loss; (b) Core loss

V. SENSITIVITY ANALYSIS OF THE PROPOSED MODEL

For model-based analysis and design, the accuracy of the model parameters have important effects on the results. In the proposed model, R_s and R_r' are functions of temperature, R_c and L_{ms}/L_m are also functions of flux levels. Meanwhile, magnetic saturation, skin effect, etc. will also affect the model parameters. These complex and nonlinear effects are not explicitly segregated as separate factors in the proposed model but can be accommodated by parameter adaptation via look-up tables or empirical equations if needed. The proposed model is applicable to different operating conditions, where the configuration/structure of the proposed model remains unchanged, but proper parameter adaptation may be needed for the corresponding operating conditions.

To study the effects of the proposed model parameters on the machine losses, a series of model parameter sensitivity tests are conducted on the 1.5HP induction machine at nine different operating conditions: three speeds (1730 RPM, 1200 RPM, 600 RPM) combined with three torques (6 N·m, 3 N·m, 1N·m) at each speed. In each simulation run, one of the six independent model parameters, R_s, L_{ls}, R_r', L_{lr}', R_c, L_m(L_{ms}), is changed by -20%, -10%, 10%, 20% of their nominal values. The results for (1735 RPM, 6 N·m), (1735 RPM, 1 N·m) and (600 RPM, 1 N·m) conditions are shown in Fig. 23, and the legend of Fig. 23 is explained in TABLE I due to limited space in the figures. It is found that, first, R_c mainly affects P_{core}; R_s and L_m(L_{ms}) mainly affect P_{Cu}; L_{ls} and L_{lr}' have minor effects on P_{core} and little effect on P_{core}; R_r' has minor effect on P_{Cu} and almost no effect on P_{core}. These effects increase as the parameter error increases. Second, the increase of load torque mainly increases P_{Cu}. Thus, ΔP_{Cu} in percentage is less sensitive to parameters' variation in high-torque condition due to the increased value of P_{Cu}. Similarly, the increase of speed increases P_{core}. Thus, ΔP_{core} in percentage is less sensitive in the high-speed condition. Third, due to the reasons in the previous point, the estimation deviation can exceed 20% in sensitive low-torque low-speed condition, while the estimation deviation is less than 10% in the relatively insensitive high-torque high-speed condition for the same changing degree of the model parameters. Fourth, the effects of the model parameters on the power loss estimation are monotonous and almost linear before saturation. Thus, if the increase of a certain parameter increases the power loss estimation, then the decrease of the same parameter will decrease the same type of the power loss estimation in a slightly different degree.

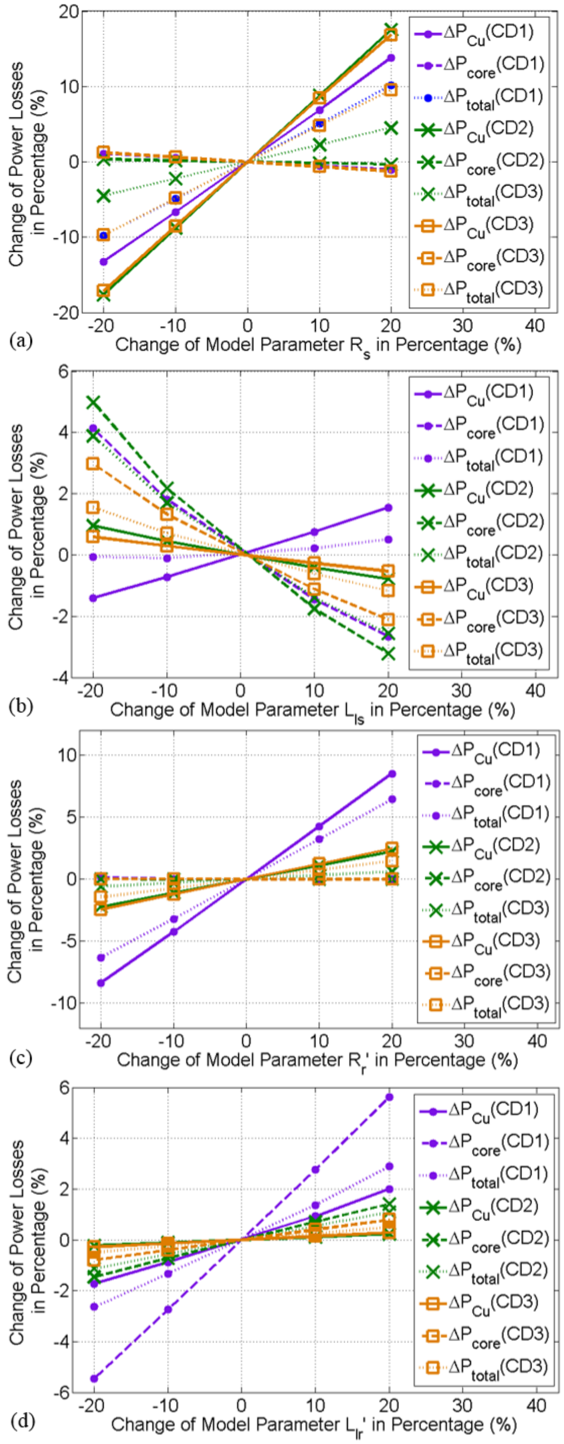

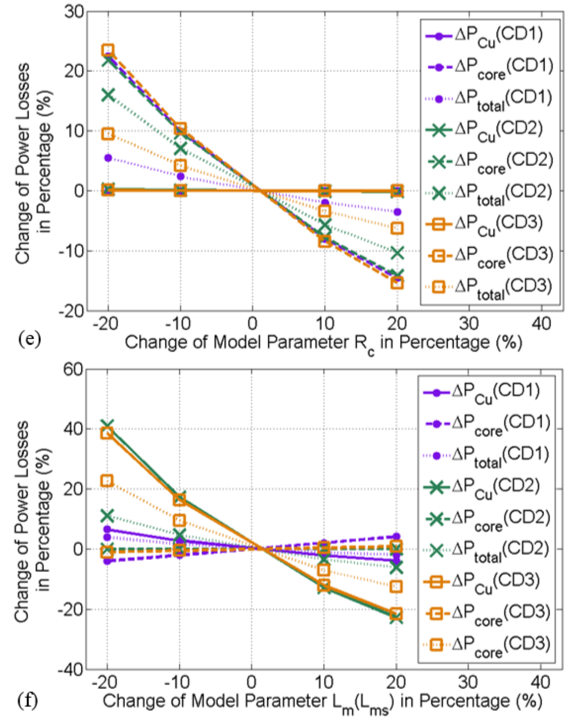

Fig. 23. Model sensitivity test results for (a) R_s; (b) L_{ls}; (c) R_r'; (d) L_{lr}'; (e) R_c; (f) $L_m(L_{ms})$. (Solid line: ΔP_{cu}; Dashed line: ΔP_{core}; Dotted line: ΔP_{total})

TALBE I. EXPLANATION OF LEGEND IN FIG. 21

	Speed	Torque	Line color + Marker
CD1 (Condition 1)	1735 RPM	6 N·m	Purple + Dot
CD2 (Condition 2)	1735 RPM	1 N·m	Green + Cross
CD3 (Condition 3)	600 RPM	1 N·m	Orange + Square

VI. CONCLUSION

This paper elaborately explained a newly proposed analytical three-phase induction machine model which is suitable for *qd0*-frame analysis and machine copper and core loss estimation at the same time. The model parameters can be conveniently extracted from the standard induction machine characterization tests at variable line frequencies. Simulation results show that the model is accurate and consistent under a changing load profile and the proposed model works for both line-fed and inverter-fed situations. The experimental validation tests are performed on three induction machines. The results show that the simulated and the experimental machine losses excellently match in the line-fed situation (>99%) and in the inverter-fed situation with machine input low-pass filters (>93%). The proposed model is also verified under flux-weakening operation to illustrate its applicability across an exemplary non-rated operating mode. Such an analytical model is expected to provide a useful tool for many studies involving advanced control design and power loss reduction of three-phase induction machines.

APPENDIX A EQUATIONS OF THE PROPOSED INDUCTION MACHINE MODEL

$$v_{qs} = R_s i_{qs} + \omega\lambda_{ds} + p\lambda_{qs}\,, \qquad \text{(A-1)}$$

$$v_{ds} = R_s i_{ds} - \omega\lambda_{qs} + p\lambda_{ds}\,, \qquad \text{(A-2)}$$

$$v_{qr}' = R_r' i_{qr}' + \left(\omega - \omega_r\right)\lambda_{dr}' + p\lambda_{qr}'\,, \qquad \text{(A-3)}$$

$$v_{dr}' = R_r' i_{dr}' - \left(\omega - \omega_r\right)\lambda_{qr}' + p\lambda_{dr}'\,, \qquad \text{(A-4)}$$

$$i_{qs} = \hat{i}_{qs} + \frac{L_{ms}}{R_c}\omega\hat{i}_{ds} + \frac{L_{ms}}{R_c}p\left(\hat{i}_{qs}\right), \qquad \text{(A-5)}$$

$$i_{ds} = \hat{i}_{ds} - \frac{L_{ms}}{R_c}\omega\hat{i}_{qs} + \frac{L_{ms}}{R_c}p\left(\hat{i}_{ds}\right), \qquad \text{(A-6)}$$

$$\lambda_{qs} = L_{ls} i_{qs} + L_m\left(\hat{i}_{qs} + i_{qr}'\right), \qquad \text{(A-7)}$$

$$\lambda_{ds} = L_{ls} i_{ds} + L_m\left(\hat{i}_{ds} + i_{dr}'\right), \qquad \text{(A-8)}$$

$$\lambda_{qr}' = L_{lr}' i_{qr}' + L_m\left(\hat{i}_{qs} + i_{qr}'\right), \qquad \text{(A-9)}$$

$$\lambda_{dr}' = L_{lr}' i_{dr}' + L_m\left(\hat{i}_{ds} + i_{dr}'\right), \qquad \text{(A-10)}$$

$$v_{0s} = R_s i_{0s} + p\lambda_{0s}\,, \qquad \text{(A-11)}$$

$$v_{0r}' = R_r' i_{0r}' + p\lambda_{0r}'\,, \qquad \text{(A-12)}$$

$$i_{0s} = \hat{i}_{0s} + \frac{L_{ms}}{R_c}p\left(\hat{i}_{0s}\right), \qquad \text{(A-13)}$$

$$\lambda_{0s} = L_{ls} i_{0s}\,, \qquad \text{(A-14)}$$

$$\lambda_{0r} = L_{lr} i_{0r}'\,, \qquad \text{(A-15)}$$

$$\omega_r = \frac{P}{2}\omega_{rm}\,, \qquad \text{(A-16)}$$

$$T_e = -\frac{pW_m}{\omega_{rm}} = \frac{3P}{4}\left(\lambda_{qr}' i_{dr}' - \lambda_{dr}' i_{qr}'\right), \qquad \text{(A-17)}$$

where ω_r, ω_{rm} and P are the rotor electrical speed, rotor mechanical speed and the number of poles, respectively.

APPENDIX B INFORMATION OF THE TESTED MACHINES

TABLE B-I. INFORMATION OF THE TESTED INDUCTION MACHINES

	Dayton 6VPE6	Dayton 6VPE8	Dayton 2MXV4
Power	1.5HP	3HP	10HP
Voltage	230 V	230 V	230 V
Current	4 A	8.1 A	25.8 A
Pole number	4	4	4
Speed	1735 RPM	1735 RPM	1755 RPM
Torque	~6.16 N·m	~12.3 N·m	~41 N·m

REFERENCES

[1] S. Ansuj, F. Shokooh, R. Schinzinger, "Parameter estimation for induction machines based on sensitivity analysis," *IEEE Trans. Ind. Appl.,* vol. 25, no. 6, pp. 1035-1040, Nov/Dec 1989.

[2] Y. Liu, A. Bazzi, "A detailed induction machine core loss model in the arbitrary reference frame," *in Proc. IEEE Applied Power Electronics Conference and Exposition* (APEC), pp. 2617-2622, 2015.

[3] A. Lamine, E. Levi, "Dynamic induction machine modelling considering the stray load losses," *in Proc. IEEE Universities Power Engineering Conference*, vol. 1, pp. 582-586, 2004.

[4] S. Nandi, "A detailed model of induction machines with saturation extendable for fault analysis," *IEEE Trans. Ind. Appl.,* vol. 40, no. 5, pp. 1302-1309, Sep/Oct. 2004.

[5] S. D. Sudhoff et al., "An induction machine model for predicting inverter-machine interaction," *IEEE Trans. Energy Convers.*, vol. 17, no. 2, pp. 203-210, Jun. 2002.

[6] J. Holtz, T. Thimm, "Identification of the machine parameters in a vector-controlled induction motor drive," *IEEE Trans. Ind. Appl.*, vol. 27, no. 6, pp. 1111-1118, Nov/Dec. 1991.

[7] A. M. Bazzi and P. T. Krein, "Review of methods for real-time loss minimization in induction machines," *IEEE Trans. Ind. Appl.*, vol. 46, no. 6, pp.2319-2328, Nov./Dec. 2010.

[8] S. J. Chapman, "Induction motors," in *Electric Machinery Fundamentals*, 5th edition, New York: McGraw-Hill, 2012, ch. 6, pp. 321.

[9] P. Krause, O. Wasynczuk, S. Sudhoff, S. Pekarek, "Symmetrical induction machines," in *Analysis of Electric Machinery and Drive Systems*, 3rd edition, New Jersey: John Wiley & Sons, 2013, ch. 6, pp. 215-266.

[10] E. Levi, "Impact of iron loss on behavior of vector controlled induction machines," *IEEE Trans. Ind. Appl.*, vol. 31, no. 6, pp. 1287-1296, Nov. 1995.

[11] G. O. Garcia, J. C. M. Luis, R. M. Stephan, E. H. Watanabe, "An efficient controller for an adjustable speed induction motor drive," *IEEE Trans. Ind. Electron.*, vol. 41, no.5, pp. 533-539, Feb. 1994.

[12] C. Chakraborty, Y. Hori, "Fast efficiency optimization technique for the indirect vector-controlled induction motor drives," *IEEE Trans. Ind. Appl.*, vol. 39, no. 4, pp. 1070-1076, Nov. 1995.

[13] M. N. Uddin and S. W. Nam, "Development of a nonlinear and model-based online loss minimization control of an IM drive," *IEEE Trans. Energy Convers.*, vol. 23, no. 4, pp. 1015-1024, Dec. 2008.

[14] E. Levi, A. Lamine, A. Cavagnino, "Impact of stray load losses on vector control accuracy in current-fed induction motor drives," *IEEE Trans. Energy Convers.*, vol. 21, no. 2, pp. 442-450, Jun. 2006.

[15] L. Cristaldi, M. Faifer, L. Piegari, M. Rossi, S. Toscani, "An analytical model of the induction machine for the development of diagnostic techniques," *in Proc. IEEE Diagnostics for Electric Machines, Power Electronics & Drives (SDEMPED)*, pp. 598-605, 2011.

[16] M. Hadjami, A. Khezzar, M. E. K. Oumaamar, H. Razik, A. Rezzoug, "Analytical model of cage induction machine dedicated to the study of axial non-uniformities," *in Proc. IEEE Diagnostics for Electric Machines, Power Electronics & Drives (SDEMPED)*, pp. 585-591, 2011.

[17] J. Muhlethaler, J. Biela, J. W. Kolar, A. Ecklebe, "Core loss under the DC bias condition based on Steinmetz parameters," *IEEE Trans. Power Electron.*, vol. 27, no. 2, pp. 953-963, Feb. 2012.

[18] I. Kioskeridis and N. Margaris, "Loss minimization in induction motor adjustable-speed drives," *IEEE Trans. Ind. Electron.*, vol. 43, no.1, Feb. 1996.

[19] A. Mannan, T. Murata, J. Tamura, T. Tsuchiya, "Efficiency optimized speed control of field oriented induction motor," in *Proc. IEEE Power Conversion Conference*, vol.3, pp. 1316-1321, 2002.

[20] J. J. C. Gyselinck et al., "Calculation of no-load induction motor core losses using the rate-dependent Preisach model," *IEEE Trans. Magn.*, vol. 34, no. 6, pp. 3876-3881, Nov. 1998.

[21] K. Yamazaki et al., "Harmonic loss and torque analysis of high-speed induction motors," *IEEE Trans. Ind. Appl.*, vol. 48, no. 3, pp. 933-941, May/Jun. 2012.

[22] W. W. Tan and H. Huo, "A generic neurofuzzy model-based approach for detecting faults in induction motors," *IEEE Trans. Ind. Electron.*, vol. 52, no. 5, pp. 1420-1427, Oct. 2005.

[23] S. A. Odhano et al., "Maximum efficiency per torque direct flux vector control of induction motor drives," *IEEE Trans. Ind. Appl.*, vol. 15, no. 6, pp. 4415-4424, Nov./Dec. 2015;

[24] J. Stumper, A. Dotlinger, R. Kennel, "Loss minimization of induction machines in dynamic operation," *IEEE Trans. Energy Convers*., vol. 28, no. 3, pp. 726-735, Sep. 2013.

[25] Z. Qu et al, "Loss-minimizing flux level control of induction motor drives," *IEEE Trans. Ind. Appl.*, vol. 48, no. 3, pp. 952-961, May/Jun. 2012.

[26] *IEEE Standard Test Procedure for Polyphase Induction Motors and Generators,* IEEE Std. 112-2004 (Revision of IEEE Std 112-1996), IEEE Power Engineering Society, 2004

[27] R. Liu, C. C. Mi, and D. W. Gao, "Modeling of eddy-current loss of electrical machines and transformers operated by pulsewidth-modulated inverters," *IEEE Trans. Magn*., vol. 44, no. 8, pp. 2021-2028, Aug. 2008.

[28] K. Bradley, W. Cao, J. Clare, and P. Wheeler, "Predicting inverter-induced harmonic loss by improved harmonic injection," *IEEE Trans. Power Electron*., vol. 23, no. 5, pp. 2619-2624, Sep. 2008

[29] A. Boglietti, P. Ferraris, M. Lazzari, and M. Pastorelli, "Influence of the inverter characteristics on the iron losses in PWM inverter-fed induction motors," *IEEE Trans. Ind. Appl*., vol. 32, no. 5, pp. 1190-1194, Sep./Oct. 1996.

[30] K. Yamazaki and N. Fukushima, "Experimental validation of iron loss model for rotating machines based on direct eddy current analysis of electrical steel sheets," *in Proc. IEEE International Electric Machines and Drives Conference*, pp. 851-857, 2009.

[31] M. Schweizer, T. Friedli, J W. Kolar, "Comparative Evaluation of advanced three-phase three-level inverter/converter topologies against two-level systems", *IEEE Ind. Electron.*, vol. 60, no. 12, pp. 5515-5527, 2013.

[32] A. Ruderman, B. Reznikov and S. Busquets-Monge, "Asymptotic time domain evaluation of a multilevel multiphase PWM converter voltage quality," *IEEE Ind. Electron.*, vol. 60, no. 5, pp. 1999-2009, 2013.